Correspondence to:
X. Shen,
xiaoteng.shen@kuleuven.be

An Approach to Modeling Biofilm Growth During the Flocculation of Suspended Cohesive Sediments

Xiaoteng Shen[1,2,3] (iD), Erik A. Toorman[2] (iD), Byung Joon Lee[4], and Michael Fettweis[5]

[1]State Key Laboratory of Estuarine and Coastal Research, East China Normal University, Shanghai, China, [2]Hydraulics Laboratory, Department of Civil Engineering, KU Leuven, Leuven, Belgium, [3]State Key Laboratory of Hydrology-Water Resources and Hydraulic Engineering, Hohai University, Nanjing, China, [4]School of Construction and Environmental Engineering, Kyungpook National University, Sangju, Gyeongbuk, Korea, [5]Operational Directorate Natural Environment, Royal Belgian Institute of Natural Sciences, Brussels, Belgium

Abstract The floc size distribution (FSD) is crucial to predict cohesive sediment dynamics in aquatic environments. Recently, increasing attention has been given to biofilm effects on the FSDs of suspended particles since the presence of biofilms on particle surfaces may lead to larger flocs and thus higher settling velocities. In this study, results from a settling column experiment conducted by Tang and Maggi (2018; https://doi.org/10.1002/2017JG004165) under nutrient-free and biomass-free, nutrient-affected and biomass-free, and nutrient-affected and biomass-affected conditions, with different suspended sediment concentrations, shear rates, and nutrient concentrations, have been used to validate modeled FSDs that is based on the population balance equation solved by the quadrature method of moments. In addition to the processes of aggregation and breakage, the effects of biofilm are expressed in the growth term of the population balance equation. The logistic growth pattern is used to account for an increase in biomass, which is primarily controlled by the specific growth rate and the carrying capacity. In this study, the biofilm growth rate is assumed nutrient dependent, and the carrying capacity of floc size is hypothesized to be proportional to the Kolmogorov microscale. With eight size classes to interpret a simulated FSD, the predicted and observed FSDs exhibit a reasonable match for all nutrient-free and biomass-free, nutrient-affected and biomass-free, and nutrient-affected and biomass-affected conditions. This simplified bioflocculation model fills the gap between the simulations of the FSDs of cohesive sediments without and with biofilms and has the potential to be included in large-scale models in the future.

Plain Language Summary In estuaries or adjacent coastal regions, the transport of suspended sediment is responsible for many environmental and engineering issues, for example, siltation and dredging in navigation channels and harbors, water quality, water clarity, pollutants transport, and ecosystem responses. Suspended sediment particles can flocculate and thus can form aggregates with size, shape, density, and settling velocity largely different from the building particles. A challenge to predict the particle behaviors originates from a lack of flocculation models that are able to address the variations in floc size distributions. The aim of this study is to develop a flocculation model that includes besides the "classical" aggregation and breakage driven by turbulence also a biological process, which is biofilm growth. The biofilm growth and its impact on flocculation and thus floc size are simulated in a similar way as the growth of microbes but with different growth rates. The model is validated with laboratory experiments that have shown that the sizes of flocs made solely with sediment particles largely increase when incubated microbes are present. This model provides a sound basis to simulate the behavior of natural particles (minerals, organic, and biological particles) and particles from human origin (plastics) in future environmental risk assessment studies.

1. Introduction

Biofilms are easily found on moist organic (e.g., decaying leaves and wood) or inorganic (e.g., submerged rocks, suspended particles, and plastic debris) surfaces. They are a collection of microorganisms (such as bacteria, algae, fungi, and protozoa) embedded in a matrix of exopolymers or extracellular polymeric substances (EPSs; Branda et al., 2005), with the term "film" referring to bacterial adhesion, aggregation, and multiplication on surfaces (Hoiby, 2017). If biofilms are referred to as the "city of microbes" (Watnick & Kolter, 2000), the EPSs represent the "house of biofilm cells" (Flemming et al., 2007). The microbes live

on the energy or nutrients from other surrounding microorganisms (Prakash et al., 2003), while the EPSs, which contribute 85–98% of the organic matter of biofilms (Flemming, 1998), can trap various organic and inorganic particles and cells such as clay, silica, debris, humic substances, and diatom cells (Riebesell, 1991).

In open-water environments, the structured biofilm communities and the secretion of EPS are a microbial adaption for ocean systems (Decho & Gutierrez, 2017). Besides biofouling (e.g., Barton et al., 2008; Delauney et al., 2010; Kerr et al., 1998; Metosh-Dickey et al., 2004; Zobell & Allen, 1935), biofilms are significantly highlighted for their influences on ecosystem health such as food web support (e.g., Saint-Béat et al., 2014), carbon and nutrient cycling (e.g., Ziegler & Lyon, 2010), photosynthetic activities (e.g., Lefebvre et al., 2011), or in determining the fate of pollutants (e.g., Quigg et al., 2016). These environmental impacts are related to the dynamics of biofilm-associated cohesive aggregates. This is because single cohesive particles are seldom present in the water columns but appear as flocs (or aggregates). During the formation of mud flocs, nutrients are adsorbed that feed species such as invertebrates in the food web. The occurrence of flocs reduces the water turbidity as compared with the constituent particles (Downing, 2006; Gibbs & Wolanski, 1992); as a result, more light is available for photosynthesis. Thus, biofilms and their excretions surrounding sediment particles considerably influence the particle sizes, shape, densities, roughness, porosities, and their settling velocities and optical signatures (Decho et al., 2003; Fettweis & Baeye, 2015; Zhao et al., 2012). At the first stage, biofilms have appeared when free-floating microorganisms collide and take roots on the surface of suspended sediment particles. This attachment is then strengthened since the microorganisms excrete slimy EPS as biological glue, which are mainly composed of polysaccharides, proteins, extracellular DNA, and lipids (Jachlewski et al., 2015). After that, the biofilms begin to grow, with their growth rate depending on various parameters such as nutrients, oxygen, temperature, and turbulence. During this stage, the biofilms act against UV (ultraviolet) light and toxic antibiotics as protective barriers of the microbes (Prakash et al., 2003). Finally, biofilm cells may also leave the surface and establish themselves in a new niche. Detachments of biofilms can be caused by hydrodynamics, predator grazing, nutrient availability, and chemical toxins (Huang et al., 2013).

In this study, attention is given to the substrates of cohesive particles (clay and silt), which have significant impacts on both engineering issues such as channel siltation (e.g., Fettweis et al., 2016; Guo et al., 2017; Song & Wang, 2013) and ecological issues such as contaminant transport (e.g., Cheng et al., 2015; Droppo et al., 2016; Li et al., 2017). Previous work has largely focused on biofilm effects on sediment stability and erodibility (e.g., Chen et al., 2017; Droppo et al., 2016); nevertheless, biofilms in suspended sediment particles also have considerable influence on fine sediment aggregation in coastal and estuarine environments. And this may lead to predictions of biased floc size distributions (FSDs) by numerical models, and thus biased settling velocities and deposition rates notably during spring and summer algae bloom periods when microorganisms are highly activated. Due to the complexity of biological effects, most numerical models only account for the mineral fraction. Examples of this approach include the one-class population balance equation (PBE) by Winterwerp (1998), the two-class model by Lee et al. (2011), the three-class model by Shen, Lee, et al. (2018), and multiclass models such as by Maggi et al. (2007) and Shen and Maa (2015, 2016a, 2017). One exception is Maggi (2009), where the organic and inorganic fractions of aggregates are represented using two single-class equations with an additional growth term to identify biomass coating, which is among the early contributions to illustrate the effects of microorganism on particle aggregation. Nevertheless, the entire FSD curve cannot be properly displayed with only one size class. Other dynamic mechanism-based models (such as Langevin dynamic model, Stokesian dynamic model, and Lattice Boltzmann model) that can reveal bioflocculation processes on a microscale but at the current stage cannot be applied in large study domains are reviewed by Lai et al. (2018).

On the other hand, experimental FSD data are valuable to validate any flocculation model. To simplify the flocculation environments, clean sediments are often employed in laboratory experiments (such as in the mixing chambers or the settling columns) in a first step to investigate the FSDs under different hydrodynamic conditions (e.g., Keyvani & Strom, 2014; Shen & Maa, 2016b, 2017; Tran & Strom, 2017). Both unimodal (e.g., Maggi et al., 2007) and multimodal (e.g., Van Leussen, 1994) FSDs are observed in the experiments. In general, the representative size of the FSD increases with increasing suspended sediment concentration (SSC). For shear rate, an increase in size is observed up to a so-called optimum shear rate, further increase results in breakage of the flocs (Dyer, 1989); nevertheless, there is another explanation

that the optimum shear rate is just the lowest shear that can keep larger flocs in suspension and shear always lead simultaneously to both collisions (which promote growth) and breakup (Zhang et al., 2019). Recently, Tang and Maggi (2016) have carried out a settling column experiment to determine the FSDs of nutrient and biomass-affected kaolinite suspensions under shear dominant conditions. A biogeochemical model was later adopted by Tang and Maggi (2018) to mimic the nitrogen cycle in suspended sediments. The purpose of our study is to predict the equilibrium or quasi-equilibrium FSDs (rather than only the representative sizes of the FSDs) of cohesive sediments, including the processes of aggregation, breakage, and biomass growth, by using a quadrature-based multiclass PBE and the observed FSDs and the measurements of time evolutions of nitrate and ammonia in Tang (2017)'s experiment. The rest of this paper is organized as follows. The flocculation model is described in section 2, with the biofilm growth term addressed in the PBE source and sink terms. In section 3, the experiments and materials to validate the model are briefly introduced. Results and discussion are presented in sections 4 and 5, respectively, and the concluding remarks are delivered in section 6.

2. Flocculation Model

2.1. Governing Equation

The PBE is essentially a conservation equation on the number density $n(\xi, t)$ of aggregates by a single or a combination of properties ξ at time t, in which ξ can be various internal features of the particles such as size, density, mass, volume, shape, and composition. In this study, the number density function defined based on particle size L (i.e., $\xi = L$) is focused on (e.g., Maggi et al., 2007; Shen & Maa, 2015; Winterwerp, 1998), since it is the fundamental property to provide critical clues of the floc settling and organisms attaching. After neglecting advection, diffusion, and settling, the governing equation of PBE in terms of the number density $n(L, t)$ of flocs with size L and at time t in a homogenous system can be expressed as (Marchisio, Pikturna, et al., 2003):

$$\frac{\partial n(L,t)}{\partial t} = -\frac{\partial}{\partial L}[G_L(L,t) \cdot n(L,t)] + A(L,t) + B(L,t), \tag{1}$$

in which $G_L(L, t)$ is the growth rate (in units of meter per second) and $A(L, t)$ and $B(L, t)$ are the aggregation and breakage source and sink terms, respectively.

It is crucial to note that although flocs are in many models assumed to mainly be composed of clay or silt-sized minerals, the nutrients and ambient microorganisms are ubiquitous in the water column (Figure 1). Phytoplankton and bacteria concentrate on the surface or interspace of the flocs, uptake the attached nutrients, and release EPS to form biofilms. The growth rate $G_L(L, t)$ in equation (1) describes nonparticulate substances that are added to the surface of a particle (Shen, 2016) with the term "growth" actually referring to biofilm growth that should be distinguished with the term "aggregation" in this study. The net increase in floc size due to biofilm effects is assumed to follow the logistic growth pattern (Tsoularis & Wallace, 2002; Maggi, 2009; Kucharavy & De Guio, 2015; Shen, Toorman, et al., 2018):

$$G_L(L,t) = \eta \cdot L \cdot \left(1 - \frac{L}{K}\right), \tag{2}$$

where η is the relative growth rate (in per second), although the word "relative" sometimes is omitted, which may nevertheless result in confusion of terminology, and K is the carrying capacity of the environment. The growth term is originally used to model crystallization of a homogeneous chemical species, like calcium crystallization in a calcium-dissolved solution. In our case, it is assumed that the biomass-sediment flocculation system is homogeneous, since it has the same building blocks. In other words, the heterogeneity is considered a property of the stable biomineral primary particles (Maggi, 2009). Based on equation (2), for a pure growth process (i.e., no aggregation or breakage) with fixed η and K, $L(t)$ simply increases monotonically to K if the initial value $L_0 < K$, while $L(t)$ declines monotonically to K if $L_0 > K$ (see curves (i) to (iv) in Figure 2a). Besides, the growth rate dL/dt has its maximum value at $L = K/2$ regardless of different L_0 (see curves (i) to (iv) in Figure 2b).

The relative growth rate η determines the time for L to approach K. On one hand, a larger η approaches the steady state K much faster; on the other hand, the growth rates dL/dt, although they also reach the local
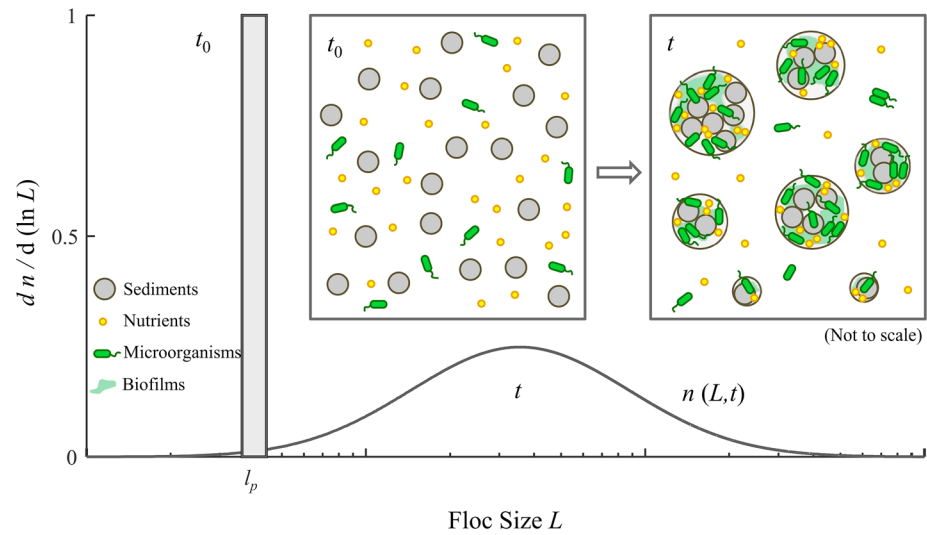
Figure 1. Schematic diagram of flocculation processes of cohesive sediments in typical aquatic environments. The time evolutions of floc size distributions are attributed to the processes of aggregation, breakage, and biofilm growth.

maximum at $L = K/2$, have larger values for a larger η if $L < K$ (see curves (i), (v), (vi), and (vii) in Figures 2a and 2b). In reality, however, the relative growth rate is often not a constant and is instead taken to be a function of the available nutrients according to the Monod equation (Monod, 1949)

$$\eta = \eta_{\max} \frac{N}{K_m + N},$$

(3)

where $\eta_{\max}$ is the maximum specific (relative) growth rate, K_m is the half-saturation concentration, and N is the nutrient concentration. Note that the nutrient concentration, more clearly, the concentration of dissolved inorganic nitrogen (DIN), can be estimated by the summation of nitrate (NO_3^-) and ammonia (NH_4^+).

The carrying capacity K in equation (2) describes the maximum floc size under a specific environment and is assumed to be proportional to the Kolmogorov length scale λ_K and relates K with the energy dissipation rate ε and the fluid kinetic viscosity ν:
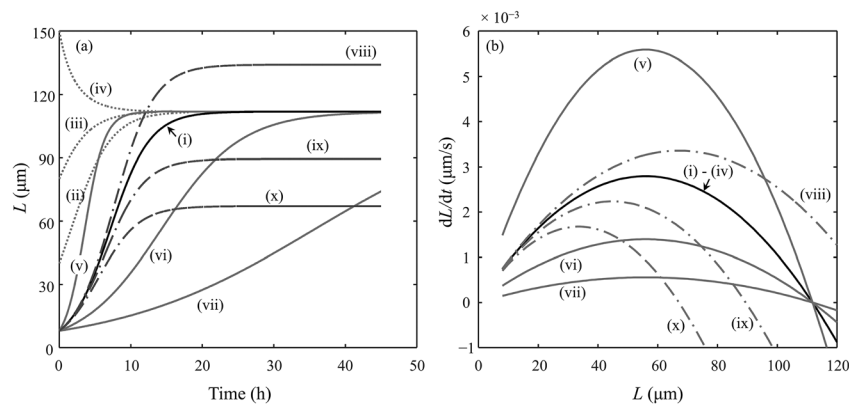

Figure 2. (a) An example of time variations of a particle with size L under shear rate $G = 80\,\mathrm{s}^{-1}$ for the logistic growth (i.e., without aggregation and breakage effects) with the following parameter values: (i) Reference curve for biomass growth rate $\eta = 1.0 \times 10^{-4}\,\mathrm{s}^{-1}$, initial particle size $L_0 = 8\,\mu\mathrm{m}$, and carrying capacity coefficient $\gamma_F = 1.0$; (ii) $\eta = 1.0 \times 10^{-4}\,\mathrm{s}^{-1}$, $L_0 = 40\,\mu\mathrm{m}$, and $\gamma_F = 1.0$; (iii) $\eta = 1.0 \times 10^{-4}\,\mathrm{s}^{-1}$, $L_0 = 80\,\mu\mathrm{m}$, and $\gamma_F = 1.0$; (iv) $\eta = 1.0 \times 10^{-4}\,\mathrm{s}^{-1}$, $L_0 = 150\,\mu\mathrm{m}$, and $\gamma_F = 1.0$; (v) $\eta = 2.0 \times 10^{-4}\,\mathrm{s}^{-1}$, $L_0 = 8\,\mu\mathrm{m}$, and $\gamma_F = 1.0$; (vi) $\eta = 5.0 \times 10^{-5}\,\mathrm{s}^{-1}$, $L_0 = 8\,\mu\mathrm{m}$, and $\gamma_F = 1.0$; (vii) $\eta = 2.0 \times 10^{-5}\,\mathrm{s}^{-1}$, $L_0 = 8\,\mu\mathrm{m}$, and $\gamma_F = 1.0$; (viii) $\eta = 1.0 \times 10^{-4}\,\mathrm{s}^{-1}$, $L_0 = 8\,\mu\mathrm{m}$, and $\gamma_F = 1.2$; (ix) $\eta = 1.0 \times 10^{-4}\,\mathrm{s}^{-1}$, $L_0 = 8\,\mu\mathrm{m}$, and $\gamma_F = 0.8$; and (x) $\eta = 1.0 \times 10^{-4}\,\mathrm{s}^{-1}$, $L_0 = 8\,\mu\mathrm{m}$, and $\gamma_F = 0.6$. (b) Plots of growth rate $\mathrm{d}L/\mathrm{d}t$ versus particle size L for the above conditions.

$$K = \gamma_F \cdot \lambda_K = \gamma_F \cdot \left(\nu^3/\varepsilon\right)^{1/4}, \tag{4}$$

in which γ_F is an coefficient accounting for other impacts that will influence K. In fact, the Kolmogorov length scale controls the ultimate floc size (Keyvani & Strom, 2014; Van Leussen, 1988). For example, in our measurements at Belgian coast, the Kolmogorov scale is always larger but proportional to the floc sizes L. Therefore, we set Kolmogorov length scale as a bound on the upper size limit of the flocs. An increment of the carrying capacity coefficient γ_F results in an increase in the carrying capacity K, and vice versa (see curves (i), (viii), (ix), and (x) in Figure 2a). The growth rates dL/dt are larger against a larger γ_F, and the maximum values of dL/dt are different since the values of γ_F, and thus $K/2$, are altered accordingly. Without a deep understanding of the behavior of the microbes and the nutrient cycling, $\gamma_F = 1.0$ is assumed at present.

The number of flocs with size L may increase when two smaller particles collide and attach to each other or may decrease when flocs with size L collide with other particles and create aggregates with size larger than L (Figure 1). Thus, the aggregation source and sink terms $A(L, t)$ can be written as

$$A(L,t) = \frac{L^2}{2}\int_0^L \left[\frac{\beta\left(\left(L^3-\lambda^3\right)^{1/3},\lambda\right)\cdot\alpha}{\left(L^3-\lambda^3\right)^{2/3}} \cdot n\left(\left(L^3-\lambda^3\right)^{1/3},t\right)\cdot n(\lambda,t)\right]d\lambda$$
$$-n(L,t)\int_0^\infty \beta(L,\lambda)\cdot a\cdot n(\lambda,t)d\lambda, \tag{5}$$

in which λ has the same dimension as L. The collision frequency β for two particles with size L and λ can be determined by equation (6) for a shear dominant environment (Camp & Stein, 1943):

$$\beta(L,\lambda) = \frac{G}{6}(L+\lambda)^3, \tag{6}$$

in which the shear rate G can be expressed by

$$G = \sqrt{\varepsilon/\nu}. \tag{7}$$

The shear rate determines also the carrying capacity K for biomass growth through equation (4). The aggregation correction factor α is a model fitting parameter accounting for particle geometry corrections β_0 ($\beta_0 = \beta_{n_f}/\beta$ in which the collision frequency β for spheres is expressed by equation (7) and β_{nf} is the collision frequency for fractal particles), contact efficiency E_0 ($E_0 \leq 1$), and attachment probability α_0 ($\alpha_0 \leq 1$) and can be written as $\alpha = \beta_0 \cdot E_0 \cdot \alpha_0$ (Shen & Maa, 2015). Note that for two particles with volume 1,000 times different (i.e., $v_j/v_i = 1000$), β_0 may be in order of 10 for $n_f \approx 2.0$ and in order of 10^2 for $n_f \approx 1.5$ (Jiang & Logan, 1991; Lee et al., 2000). Thus, the correction factor α could be larger than one for fractal particles.

The breakage source and sink term $B(L, t)$ in equation (1) describes the birth of flocs with size L from the split of a larger particle and the decrease of the number of flocs with size L due to the breakage of the floc itself. Thus, the term $B(L, t)$ can be formulated as

$$B(L,t) = \int_L^\infty a(\lambda)\cdot b(L|\lambda)\cdot n(\lambda,t)d\lambda - a(L)\cdot n(L,t), \tag{8}$$

in which a is the breakup frequency function (Winterwerp, 1998)

$$a(L) = E_b \cdot \left(\frac{\mu}{F_y}\right)^{1/2} \cdot G^{3/2} \cdot L \cdot \left(\frac{L}{l_p}-1\right)^{3-n_f}, \tag{9}$$

where E_b is a breakage fitting parameter, μ is the fluid dynamic viscosity, F_y is the floc strength, l_p is the representative size of primary particles, and n_f is the fractal dimension. Possible improvements of equation (9) can be found in Kuprenas et al. (2018).

Moreover, the fragmentation distribution function $b(L|\lambda)$ illustrates the distribution of the resulting daughter particles after a parent particle λ is destroyed. The binary (equation (10)), ternary (equation (11)), and

uniform (equation (12)) distributions may be selected based on the observed FSD under different conditions (Shen & Maa, 2016a).

$$b(L|\lambda) = \begin{cases} 2 & L = \lambda/2^{1/3} \\ 0 & \text{otherwise} \end{cases}, \tag{10}$$

$$b(L|\lambda) = \begin{cases} 1 & L = \lambda \cdot (1/2)^{1/3} \\ 2 & L = \lambda \cdot (1/4)^{1/3} \\ 0 & \text{otherwise} \end{cases}, \tag{11}$$

$$b(L|\lambda) = 6L^2/\lambda^3 \quad (0 < L < \lambda). \tag{12}$$

Notice that the binary breakup accounts for a parent particle λ breaking up into two particles with volume ratio 1:1, the ternary breakup represents a parent particle λ splitting into three smaller particles with volume ratio 1:1:2, and the uniform breakage describes the daughter particles with any size $(0, \lambda)$ having the same number.

2.2. Solution Method

The quadrature method of moments is adopted to solve the governing equation (equation (1)), with the growth rate given in equation (2), and the aggregation and breakage terms expressed by equations (5) and (8). Providing that the FSD is represented by a series of delta functions (McGraw, 1997),

$$n(L,t) = \sum_{i=1}^{N_d} w_i(t)\delta[L - L_i(t)], \tag{13}$$

in which N_d is the number of size classes and L_i and w_i ($i = 1, 2, \ldots, N_d$) are the representative size and the corresponding weight of each class; the FSD information can be stored in its moments defined by

$$m_{k/p} = \int_0^\infty L^{k/p} n(L,t) dL = \sum_{i=1}^{N_d} w_i L_i^{k/p}, \tag{14}$$

in which p is the adjustable factor and $m_{k/p}$ is the (k/p)th-order moment of the number density function $n(L, t)$. Note that the regular moments m_0, m_1 (i.e., $k = p$), and m_2 (i.e., $k = 2p$) are proportional to the total number, length, and surface area, respectively. In particular, the moment m_3 (i.e., $k = 3p$) represents the total solid volume of the flocs (V), which implicitly consists of two sections: the mineral solid volume (V_M) and the biomass volume (V_B; Maggi, 2009). The number based mean size $d_{1,0}$ can be calculated as $d_{1,0} = m_1/m_0$.

By applying the moment transformation (equation (14)) for the governing equation (equation (1)), the moment equation can be simplified to (Shen & Maa, 2015; Su et al., 2007):

$$\frac{\partial m_{k/p}}{\partial_t} = \frac{1}{2}\sum_{i=1}^{N_d}\omega_i\sum_{j=1}^{N_d}\alpha(L_i, L_j)\cdot\beta(L_i, L_j)\cdot\omega_j\cdot\left(L_i^3 + L_j^3\right)^{\frac{k}{3p}}$$
$$-\sum_{i=1}^{N_d}L_i^{k/p}\omega_i\sum_{j=1}^{N_d}\alpha(L_i, L_j)\cdot\beta(L_i, L_j)\cdot\omega_j + \sum_{i=1}^{N_d}a_i\overline{b_i}^{(k/p)}\omega_i - \sum_{i=1}^{N_d}L_i^{k/p}a_i\omega_i \tag{15}$$
$$+\frac{k}{p}\sum_{i=1}^{N_d}w_i\cdot G_L(L_i)\cdot L_i^{(k/p)-1},$$

in which

$$\overline{b_i}^{(k/p)} = \int_0^\infty L^{k/p} b(L|\lambda) dL. \tag{16}$$

It is essential to note that with the assumption of binary (equation (10)), ternary (equation (11)), and uniform (equation (12)) breakup, the integral in $\overline{b_i}^{(k/p)}$ can be expressed by equations (17), (18), and (19), respectively (Shen & Maa, 2016a).

$$\overline{b}_i^{(k/p)}(L) = 2^{(3-k/p)/3}L^{k/p}, \tag{17}$$

$$\overline{b}_i^{(k/p)}(L) = L^{k/p}\left(2^{\frac{-k}{3p}} + 2^{1-\frac{2k}{3p}}\right), \tag{18}$$

$$\overline{b}_i^{(k/p)}(L) = \frac{6p}{k+3p}L^{k/p}. \tag{19}$$

At each time t, when the first $2 \cdot N_d$ moments (i.e., $m_0, m_{1/p}, \dots m_{[2\cdot Nd\ -1]/p}$) are available, the FSD can be displayed by N_d size groups with their representative sizes L_i and corresponding weights w_i ($i = 1, 2, \dots, N_d$), by using the Wheeler's algorithm (Wheeler, 1974) to find the eigenvalues and eigenvectors of a real, symmetric and tridiagonal Jacobi matrix within which the elements are represented by the moments at time ($t-dt$). Thus, the moments can be renewed, after the source and sink terms (right-hand side of equation (15)) are updated with computed L_i and w_i. With the adjustable factor $p = 3$ to alleviate the ill condition of the above Jacobi matrix, eight size classes (i.e., $N_d = 8$) are guaranteed to present the equilibrium FSD and thus is used for all cases in this study. Notice that at $t = 0$, all particles are assumed concentered around the median size of primary particles l_p (i.e., $N_d = 1$). The program will spread the initial point distribution to multiclass distribution by checking both the minimum distance of adjacent sizes and the ratio of minimum and maximum weights (Shen & Maa, 2015; Yuan & Fox, 2011).

3. Materials and Methods

3.1. Experimental Setup

The settling column test carried out by Tang (2017) was employed to validate this flocculation model. Thus, an overview of the experimental conditions from Tang (2017) is presented here to provide context for the modeling analysis. As shown in Figure 3a, the transparent Perspex column, with a cross-section of 210 mm × 140 mm and a height of 870 mm, was divided into three sections: the settling section, the water quality measuring section, and the FSD measuring section (Tang & Maggi, 2015). All the three sections were filled with tap water during the experiment. The settling section (140 mm × 140 mm × 600 mm) was the place for fine sediment suspensions colliding, aggregating, and falling. Oscillating grids were used to generate approximately isotropic and homogenous turbulence fields with average shear rates ranging from 32 to 96 s^{-1}. The water quality measuring section (70 mm × 140 mm × 600 mm) was partitioned within the settling section by a vertical separator to provide space for a water quality meter that measures parameters such as the concentration of nitrate (NO_3^-), ammonium (NH_4^+), and dissolved oxygen (Tang & Maggi, 2015). A triangular slope at the bottom of this section allowed deposited sediments to transport to the settling section by turbulence. The FSD measuring section was located at the bottom of the column (210 mm × 140 mm × 270 mm height), separated by a diaphragm with a few 5-mm sampling holes for flocs passing through.

Tang (2017) tested three different sediment concentrations $c_k = \{0.1, 0.2, 0.4\}$ g/L in the settling column experiments. For each SSC, seven different sediment types were used under the broader categories of (i) nutrient-free and biomass-free (NFBF); (ii-iv) nutrient-affected and biomass-free (NABF), with NH_4NO_3 concentrations 1.5, 3.0, and 6.0 mM; and (v-vii) nutrient-affected and biomass-affected (NABA) conditions, also with the above NH_4NO_3 concentrations. The NFBF and NABF samples were prepared using only kaolinite (type Q38, with primary particles ranging in size from 0.6 to 38 μm), while the NABA samples were incubated with natural sediment collected from Blackwattle Bay (Sydney, Australia) for 21 days at 21 °C before the start of the experiments. For each independent condition, the grid oscillation frequency was initially set so that $G = 32$ s^{-1} and then increased every 3 hr according to the following pattern: $G = \{32, 48, 64, 80, 96\}$ s^{-1} (Figure 3b). During the FSD measuring period, the grids were temporally stopped to allow the particles to settle to the image acquisition section. Note that the flocs may have time to grow when the grid was turned off and when the flocs were measured, which should be noticed in future experiments. The floc images were acquired by the micro particle image velocimetry (μPIV) system, which consists of an imaging system and an illumination system that produced image resolutions of 0.375 to 4.435 μm^2 per pixel with magnification ratios ranging from 0.58 to 7. The FSDs around time $t = \{3, 6, 9, 12, 15\}$ hr before grid frequency changing were thus processed to show the equilibrium or quasi-equilibrium FSDs under shear rates $G = \{32, 48, 64, 80, 96\}$ s^{-1} for different environments. The reported FSDs as well as their representative sizes
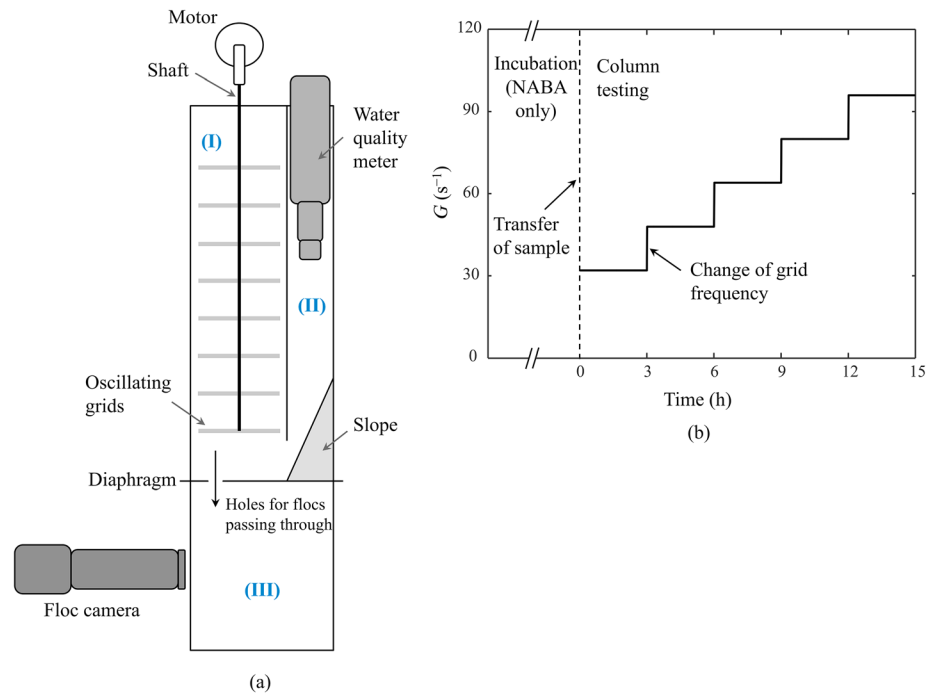
Figure 3. Laboratory system of Tang (2017) for flocculation tests. (a) The experimental facility: (I) the settling section, (II) the water quality measuring section, and (III) the floc size distribution measuring section. (b) Sequence of shear rates in the experiments. The shear rates increase every 3 hr by changing the frequency of oscillating grids. The sediments are incubated before transferring into the settling column for nutrient-affected and biomass-affected (NABA) conditions, whereas the samples are not incubated for nutrient-free and biomass-free and nutrient-affected and biomass-free conditions.

were adopted to compare with the model predictions. More details can be found in Tang and Maggi (2015, 2016) and Tang (2017).

3.2. Model Setup

For the NABA conditions, the time series of measured DIN concentrations (i.e., concentrations of NO_3^- and NH_4^+) for $c_k = \{0.1, 0.2, 0.4\}$ g/L (Figure 4) are used as model inputs to estimate the relative growth rate of biomass (η). The initial concentrations of NH_4NO_3 in the beakers before incubation are 1.5, 3.0, and 6 mM (M = mol/L), respectively. The nutrients are consumed over time and diluted when the incubations are transferred to the settling column that is filled with 15-L tap water. For NABF conditions, assuming no adsorption and no consumption, the final DIN concentration in the column should be 0.1, 0.2, and 0.4 mM. This is, however, not fully met, for example, for $c_k = 0.4$ g/L or for $c_k = \{0.1, 0.2\}$ g/L and an initial NH_4NO_3 concentration of 3.0 mM (Figure 4). The effects of ionic concentrations are represented in the model by selecting different correction factor α. The DIN concentration under NFBF condition is not zero (<0.1 mM), due to the use of tap water in the settling column.

The maximum specific growth rate η_{max}, and thus the relative growth rate η, is set as null for the NFBF and NABF conditions. For the NABA conditions, η_{max} is determined by shifting the D_{50} (median size) $\sim t$ curve at NABF condition to the corresponding NABA condition with the same sediment concentration c_k and nutrient concentration N, since the measured D_{50} at $t = \{3, 6, 9, 12, 15\}$ hr for both conditions are available. A constant η_{max} is used for all shear rates for the same SSC and nutrient conditions. As typical values in estuaries and coastal waters, the half saturation parameter K_m for DIN is selected as 1.0×10^{-6} M (Maggi, 2009), the median size of primary particles (l_p) is chosen as 8 μm (Tang, 2017), and an averaged fractal dimension (n_f) of 2.0 (e.g., Lee et al., 2011; Maggi, 2009; Winterwerp, 1998) is applied for all cases. The breakage coefficient (E_b) is fixed as 2.0×10^{-5} to make the flocculation intensity based on the aggregation correction factor α, since Shen and Maa (2016a) indicate that the same ratio of α/E_b will result in the same prediction of
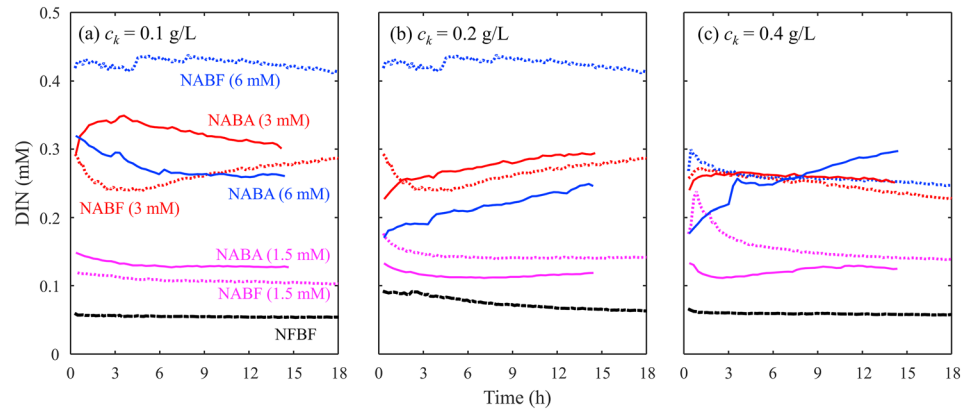
Figure 4. Time variations of measured dissolved inorganic nitrogen (DIN) concentrations for suspended sediment concentrations (a) 0.1, (b) 0.2, and (c) 0.4 g/L, respectively (Tang & Maggi, 2018). For each suspended sediment concentration, seven kaolinite samples are prepared: (i) nutrient-free and biomass-free (NFBF) and (ii–vii) nutrient-affected and biomass-free (NABF) and nutrient-affected and biomass-affected (NABA) with initial nutrients 1.5, 3.0, and 6.0 mM, respectively.

equilibrium FSD for aggregation and breakage processes. This selection also ensures that the FSD in the model arrives at equilibrium or quasi-equilibrium state before the shear rate changes (i.e., within 3 hr). The errors of predicted and observed FSDs are calculated by (Maggi et al., 2007; Shen & Maa, 2017)

$$E = \frac{1}{2}\left(\sum_{i=1}^{N_d}\left|w_{i,M}-w_{i,E}\right|\right), \tag{20}$$

where $\sum_{i=1}^{N_d} w_{i,M} = 1$, $\sum_{i=1}^{N_d} w_{i,E} = 1$, and w_{Mi} and w_{Ei} are modeled and experimental weights at L_i ($i = 1, 2, \dots, N_d$). Other model parameters and the FSD prediction errors under NFBF, NABF, and NABA conditions are shown in Tables 1 and 2.

4. Results

In this section, simulation results of the equilibrium or quasi-equilibrium FSDs for different SSC, shear rates and nutrient concentrations are compared with the experimental data. Selected FSD results were shown in section 4.1, and sensitivities of key calibration parameters were illustrated in section 4.2.

4.1. FSD Predictions

Consider, for example, when the SSC is 0.1 g/L, the predicted FSDs for shear rate $G = \{32, 48, 64, 80, 96\}\,\text{s}^{-1}$, under NFBF, NFBA, and NABA conditions with initial NH_4NO_3 concentration 3.0 mM, represent a reasonable match with the observed FSDs (Figure 5a). For NFBF condition, the FSDs at $G = \{32, 48, 64\}\,\text{s}^{-1}$ are predicted using the same parameters (Table 1), that is, $\alpha = 2.1$ and $\overline{b}_i^{(k)}$ for binary breakage, with the FSD under $G = 32\,\text{s}^{-1}$ for calibration and the FSDs under $G = \{48, 64\}\,\text{s}^{-1}$ for validations. For $G = \{80, 96\}\,\text{s}^{-1}$, the ternary and uniform fragmentation distribution functions are used, respectively, to fit wider spread FSDs, and thus, the parameter α is recalibrated accordingly. Note that the mechanism to describe the daughter particle distribution after a parent floc splitting is unclear. It is difficult to observe $\overline{b}_i^{(k)}$ directly, and therefore, $\overline{b}_i^{(k)}$ is often determined based on assumptions and validated by fitting the measured FSD (e.g., Lee et al., 2011; Mietta et al., 2008; Shen & Maa, 2016a). Some predicted size classes are smaller than the median primary particle size, l_p, especially the size of the first class under $G = 96\,\text{s}^{-1}$. For NABF

Table 1
Model Parameters, the Predicted Median Sizes (D_{50P}), and the FSD Errors (E), for the NFBF Conditions Under SSC $c_k = \{0.1, 0.2, 0.4\}$ and Shear Rates $G = \{32, 48, 64, 80, 96\}\,s^{-1}$

c_k (g/L)	G (s^{-1})	α	$\overline{b}_i^{(k)}$	D_{50P} (µm)	E
0.1	32	2.1	Binary	23.6	0.04
	48	2.1	Binary	22.7	0.13
	64	2.1	Binary	21.4	0.08
	80	2.1	Ternary	13.5	0.06
	96	1.0	Uniform	10.1	0.10
0.2	32	1.7	Binary	29.8	0.05
	48	1.7	Binary	27.6	0.06
	64	1.7	Uniform	18.8	0.13
	80	1.7	Uniform	18.0	0.15
	96	1.7	Uniform	17.4	0.06
0.4	32	0.8	Binary	29.0	0.06
	48	2.9	Ternary	28.6	0.08
	64	0.8	Binary	25.4	0.09
	80	0.5	Ternary	13.3	0.06
	96	0.5	Ternary	12.8	0.11

Note. FSD = floc size distribution; NFBF = nutrient-free and biomass-free; SSC = suspended sediment concentration.

Table 2
Model Parameters, the Predicted Median Sizes (D_{50P}), and the FSD Errors (E), for the NABF and NABA Conditions Under SSC c_k = {0.1, 0.2, 0.4}, Nutrient Concentration N = {1.5, 3.0, 6.0} mM, and Shear Rates G = {32, 48, 64, 80, 96} s⁻¹

NABF								NABA							
c_k (g/L)	N (mM)	G (s⁻¹)	α	$\overline{b_i}^{(k)}$	η_{max} (s⁻¹)	D_{50P} (μm)	E	c_k (g/L)	N (mM)	G (s⁻¹)	α	$\overline{b_i}^{(k)}$	η_{max} (s⁻¹)	D_{50P} (μm)	E
0.1	1.5	32	3.4	Binary	0	29.9	0.04	0.1	1.5	32	8.5	Uniform	1.5×10⁻⁵	35.4	0.11
		48	3.4	Binary		27.6	0.08			48	3.8	Binary		35.0	0.11
		64	3.4	Binary		26.1	0.14			64	6.2	Binary		43.8	0.10
		80	3.4	Uniform		18.0	0.06			80	7.2	Ternary		28.6	0.09
		96	3.4	Uniform		17.4	0.09			96	1.0	Uniform		16.0	0.13
0.1	3.0	32	2.8	Binary	0	27.1	0.08	0.1	3.0	32	14.5	Ternary	1.7×10⁻⁵	37.7	0.10
		48	2.8	Binary		25.6	0.07			48	14.5	Ternary		37.1	0.07
		64	2.8	Binary		24.0	0.05			64	2.8	Binary		31.9	0.13
		80	6.0	Ternary		19.8	0.11			80	6.0	Ternary		27.9	0.10
		96	2.8	Uniform		16.1	0.04			96	2.8	Uniform		24.5	0.09
0.1	6.0	32	3.5	Binary	0	30.3	0.15	0.1	6.0	32	13.5	Ternary	2.0×10⁻⁵	37.3	0.14
		48	3.5	Binary		28.0	0.11			48	9.0	Ternary		32.1	0.13
		64	7.5	Ternary		22.5	0.08			64	9.0	Ternary		32.8	0.10
		80	5.0	Ternary		18.4	0.07			80	7.5	Ternary		31.3	0.07
		96	3.5	Uniform		17.6	0.05			96	5.0	Ternary		27.6	0.07
0.2	1.5	32	1.8	Binary	0	30.6	0.05	0.2	1.5	32	6.5	Ternary	1.0×10⁻⁵	34.6	0.08
		48	1.8	Binary		28.4	0.06			48	2.0	Binary		33.9	0.10
		64	1.8	Binary		26.7	0.13			64	2.0	Binary		34.1	0.09
		80	3.5	Ternary		21.0	0.06			80	2.0	Binary		34.2	0.07
		96	3.0	Uniform		21.9	0.09			96	2.0	Uniform		24.6	0.08
0.2	3.0	32	1.8	Binary	0	30.6	0.05	0.2	3.0	32	5.5	Ternary	1.0×10⁻⁵	32.7	0.10
		48	1.8	Binary		28.4	0.06			48	4.5	Ternary		29.3	0.07
		64	1.8	Binary		26.7	0.10			64	2.5	Binary		37.1	0.10
		80	3.5	Ternary		21.0	0.08			80	1.8	Binary		32.6	0.10
		96	3.0	Uniform		21.9	0.08			96	3.5	Ternary		26.4	0.05
0.2	6.0	32	1.8	Binary	0	30.6	0.07	0.2	6.0	32	8.0	Ternary	1.0×10⁻⁵	37.6	0.11
		48	1.8	Binary		28.4	0.05			48	7.7	Ternary		35.4	0.08
		64	1.8	Binary		26.7	0.09			64	6.2	Ternary		31.7	0.10
		80	3.5	Ternary		21.0	0.10			80	2.8	Uniform		26.5	0.04
		96	3.0	Uniform		21.9	0.10			96	2.8	Ternary		23.1	0.08
0.4	1.5	32	1.0	Binary	0	32.1	0.08	0.4	1.5	32	2.3	Uniform	1.0×10⁻⁵	35.6	0.15
		48	2.3	Ternary		26.0	0.08			48	2.3	Ternary		29.1	0.08
		64	1.0	Binary		27.9	0.08			64	3.6	Ternary		34.0	0.09
		80	4.8	Ternary		31.8	0.07			80	1.2	Binary		35.3	0.10
		96	2.3	Ternary		22.6	0.05			96	1.3	Ternary		22.9	0.04
0.4	3.0	32	0.92	Binary	0	30.9	0.08	0.4	3.0	32	3.2	Uniform	1.0×10⁻⁵	40.8	0.13
		48	0.92	Binary		28.5	0.04			48	3.2	Ternary		32.8	0.10
		64	0.92	Binary		26.9	0.10			64	3.6	Ternary		33.3	0.10
		80	0.92	Binary		25.7	0.10			80	0.9	Binary		30.8	0.08
		96	0.92	Binary		24.7	0.12			96	2.2	Ternary		27.6	0.05
0.4	6.0	32	1.9	Binary	0	31.4	0.05	0.4	6.0	32	12.0	Ternary	1.0×10⁻⁵	44.6	0.11
		48	4.7	Ternary		26.2	0.12			48	10.0	Ternary		38.9	0.08
		64	1.9	Binary		27.3	0.08			64	7.2	Ternary		32.9	0.08
		80	1.9	Binary		26.1	0.05			80	3.6	Ternary		25.0	0.09
		96	1.9	Binary		25.1	0.08			96	1.0	Binary		24.5	0.06

Note. FSD = floc size distribution; NABF = nutrient-affected and biomass-free; NABA = nutrient-affected and biomass-affected; SSC = suspended sediment concentration.

conditions (Figure 5a), the FSDs under G = {32, 48, 64} s⁻¹ are predicted with binary breakage and α = 2.8, which is 33% larger than α in NFBF conditions (Table 2). This is most likely due to the electrical double layer depressed with more ions around that result in a larger probability of attachments (Shaw, 1992; see also Lintern, 2003; Sobeck & Higgins, 2002). Under G = {80, 96} s⁻¹, again the ternary and uniform $\overline{b_i}^{(k)}$ are selected, with the parameter α around two times larger than α used in NFBF cases. For NABA conditions (Figure 5a), the maximum specific growth rate (η_{max}) of flocs is selected as 1.7×10⁻⁵ s⁻¹ (Table 2), which
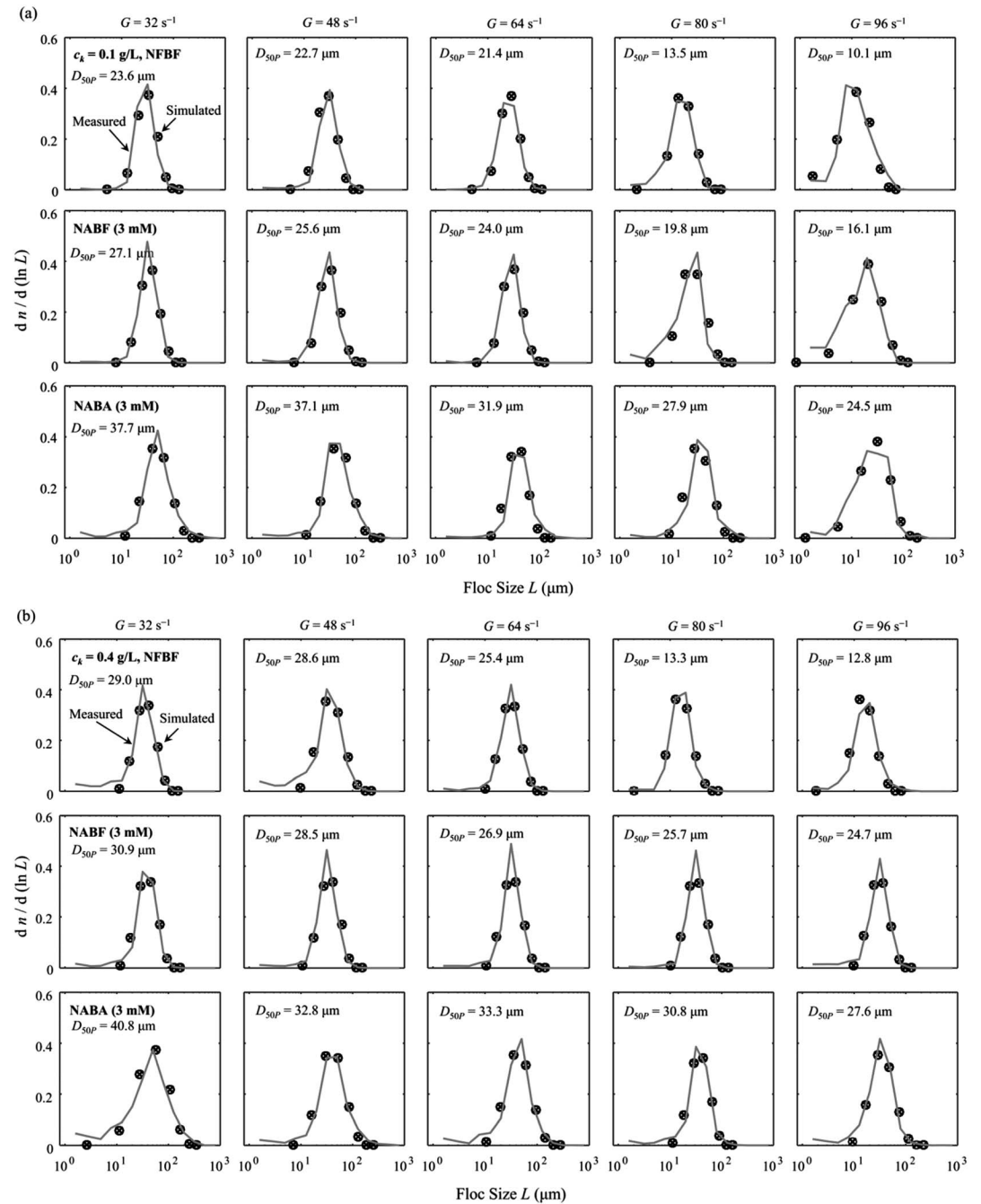
Figure 5. Examples of predicted floc size distributions (symbols) against measurements (lines) for sediment concentrations of (a) $c_k = 0.1$ g/L and (b) $c_k = 0.4$ g/L. In each subfigure, the rows represent conditions of (i) nutrient-free and biomass-free (NFBF), (ii) nutrient-affected and biomass-free (NABF) with $N = 3.0$ mM, and (iii) nutrient-affected and biomass-affected (NABA) with $N = 3.0$ mM, and different columns are for shear rates 32, 48, 64, 80, and 96 s^{-1}, respectively. The predicted median sizes D_{50P} are represented for comparison.

is roughly 1 order of magnitude smaller than the growth rate of microbes (Maggi, 2009). For the same $\overline{b}_i^{(k)}$ chosen for NABF and NABA conditions under $G = \{64, 80, 96\}$ s^{-1}, the same α is used; nevertheless, α is readjusted for NABA condition under $G = \{32, 48\}$ s^{-1} since the ternary breakage is applied instead to match a wider FSD. The results in Figure 5a also show that the spread of FSDs under low shear is narrow while under high shear is relatively wide when biofilm is absent; nevertheless, the spread is narrow at median shear while relatively wide at low and high shear rates when microbes are abundant. In this case,
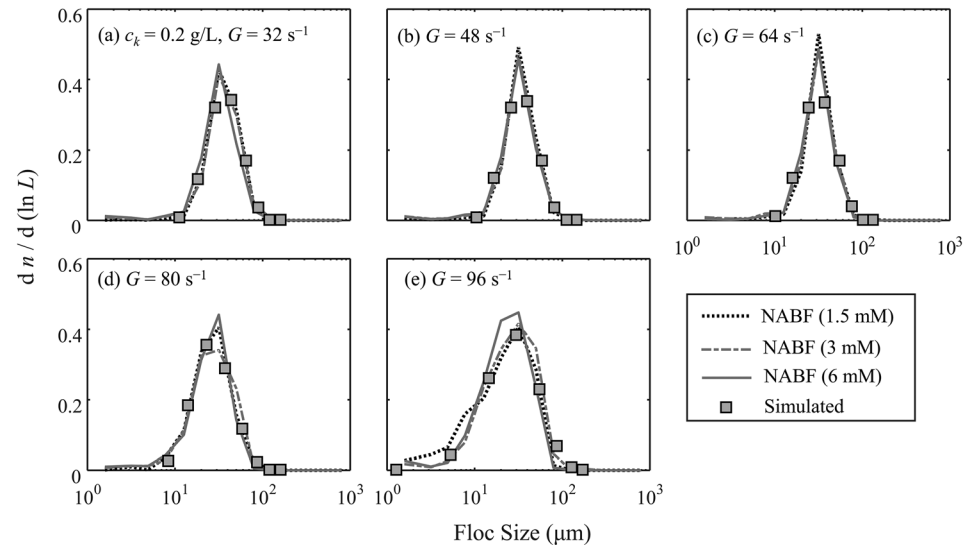
Figure 6. Predicted floc size distributions (symbols) under different shear rates $G = \{32, 48, 64, 80, 96\}$ s^{-1} for nutrient-affected and biomass-free (NABF) conditions with SSC 0.2 g/L. The observed floc size distributions (lines) with different nutrients are close, and thus, they are simulated by using the same parameters.

the aggregation correction factor α is often larger than one in this study. This is because the collision frequency β expressed by equation (6) may be largely underestimated due to their fractal properties, which should be corrected in α (Shen & Maa, 2015). The median size (D_{50}) of the FSD decreases with an increase in shear rate, slightly increase with nutrients added, and are remarkably enlarged with incubated microbes. The errors (E) (equation (20)) of FSDs shown in Figure 5a are between 0.04 and 0.13, which shows better predictions than E given in Maggi et al. (2007) ranging from 0.11 to 0.21.

Keeping the same N but increasing c_k to 0.4 g/L, the simulated FSDs also agree well with the measured FSDs for NFBF, NABF, and NABA conditions with various shear rates (Figure 5b). For NFBF conditions, $\alpha = 0.8$ is applied under $G = \{32, 64\}$ s^{-1} for binary breakup while $\alpha = 0.5$ is used under $G = \{80, 96\}$ s^{-1} for ternary breakup. Under $G = 48$ s^{-1}, even the model is recalibrated, it is difficult to address the long tail of FSD curve for particles less than 10 μm. This part could be improved by selecting a better fragmentation distribution function in the future. Note that, usually, the same α should be used for all shear rates in similar environments if the same $\overline{b}_i^{(k)}$ is selected (e.g., Maggi et al., 2007; Shen & Maa, 2015). Therefore, a value of $\alpha = 0.92$ with binary breakup are applied for all shear rates under NFBA conditions to represent narrow spread FSDs throughout (Figure 5b). Although the observed peak floc size is difficult to be accurately captured, it locates between the simulated L_3 and L_4. Thus, the deviations of the FSD predictions are not significant. For NABA conditions (Figure 5b), the maximum specific growth rate $\eta_{max} = 1.0 \times 10^{-5}$ s^{-1} is imposed for all shear rates. Then, the daughter distribution functions $\overline{b}_i^{(k)}$ are changed with the parameter α determined accordingly. Similar as that shown for NABA conditions in Figure 5a, a narrow spread FSD appears under median shear (i.e., $G = 80$ s^{-1} in this case), while larger spread FSDs are observed under lower or higher shear rates.

The results also show that in general, the FSDs under NABF conditions for the same c_k and G are close, regardless of the nutrient concentrations. For example, the FSDs under different initial NH$_4$NO$_3$ concentrations are modeled using the same α and $\overline{b}_i^{(k)}$ (Figure 6), with the maximum FSD error $E = 0.13$ (Table 2). It agrees with the observed FSDs in a mixing jar experiment by Shen and Maa (2016b) who use the same curve to mimic the FSDs under salinity 0.5, 1.0, 2.0, 3.0, 5.0, and 9.0.

4.2. Sensitivity Tests

In order to understand the relationships between various calibration parameters and the model predictions, the biomass-affected FSDs under $C_k = 0.2$ g/L and $N = 1.5$ mM were further tested, with the best-fit model
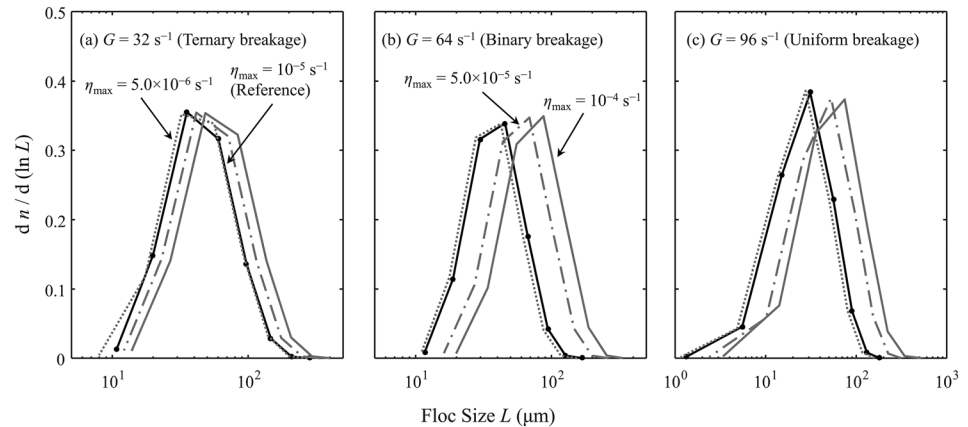
Figure 7. Sensitivities of the maximum specific growth rate η_{max} for floc size distributions under (a) low, (b) moderate, and (c) high shear rates. The suspended sediment concentration is 0.2 g/L, and the biological effects are included with nutrient concentration 1.5 mM.

used as a reference (see dark solid line shown in Figure 7). The ternary, binary, and uniform breakage patterns are selected under low, middle, and high shear rates (i.e., $G = \{32, 64, 96\}$ s^{-1}), respectively, to better match the spread of observed FSDs. For all shear rates, the predicted FSD curve shifts to the right (or left) for a larger (or smaller) value of the maximum specific growth rate (η_{max}), nevertheless with nearly no changes of the shape of the FSDs (Figure 7). The example also indicates the growth of flocs to both mineral particles aggregation and biofilms attachments. The FSDs are more sensitive with the alteration of η_{max} under middle shear with binary breakage (Figure 7b) than the condition under low or high shear with ternary or uniform breakage (Figures 7a and 7c). Additionally, it is interesting to point out that the model simulated FSDs are not sensitive with the selections of the carrying capacity coefficient γ_F for the cases represented in this study. This is because with a meaningful value of η_{max} of the order of 10^{-5} s, the model does not reach an equilibrium state within the duration of the experiment. In estuary and coastal environments, however, the flocs could have sufficient time to grow with their upper bound controlled by both hydrodynamic conditions (by Kolmogorov microscale λ_K) and other unknown influences (by coefficient γ_F).

5. Discussion

5.1. The Necessity of a Biofilm Growth Term in a Flocculation Model

It would also be good to know if the same results (i.e., FSDs and their representative sizes) could have been produced with the original Shen and Maa (2015)'s model if it were calibrated to the data. The main difference between both models is that Shen and Maa (2015)'s model does not have the biofilm growth term (i.e., the last term on the right-hand side of equation (15)) and thus only deals with clean sediments (i.e., $\eta = 0$). One experiment with $c_k = 0.1$ g/L and initial NH$_4$NO$_3$ 3.0 mM under the NABA condition is selected in order to investigate the differences in results between both models. In fact, with the correction factors $\alpha = \{20.0, 20.0, 7.5, 15.0, 7.5\}$ for shear rates $G = \{32, 48, 64, 80, 96\}$ s^{-1}, respectively, the FSDs can be reasonably simulated with the Shen and Maa (2015)'s model with the errors of FSDs ranging from 0.07 to 0.11. However, α used in their model is significantly larger than α in this study (Table 2). This is because in the Shen and Maa (2015) model the floc size can only increase due to collision and aggregation, whereas in our model the aggregates can also grow because of biofilm coating. At current stage, it is difficult to judge if such a large α in Shen and Maa (2015) model is still meaningful when considering the fractal properties of flocs.

More obvious differences between both models can be shown from the plots of time evolution of the moments and their representative sizes (Figure 8). In this study, the moments of FSDs arrive at new quasi-equilibrium state after the shear rate changes at $t = \{3, 6, 9, 12, 15\}$ hr (solid lines in Figure 8a). The third regular moment m_3, which represents total solid volume ($V = V_M + V_B$) increases due to biofilm attachments that combine nonparticulate organism within sediment aggregates. In Shen and Maa (2015)'s model,
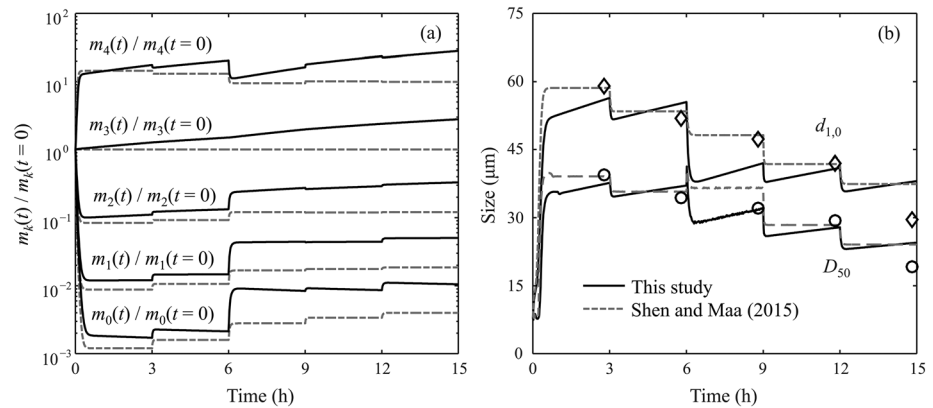
Figure 8. Time variations of (a) simulated moments of floc size distributions and (b) predicted mean and median sizes (i.e., $d_{1,0}$ and D_{50}) against measurements (symbols), for nutrient-affected and biomass-affected condition with suspended sediment concentration $c_k = 0.1$ g/L and nutrient concentration $N = 3.0$ mM. The observations are also recalibrated by using Shen and Maa (2015)'s model for comparison (dashed line).

however, the total solid volume ($V = V_M$) is conserved and unchanged, which results in smaller values of m_k in their simulations (dashed lines in Figure 8a). The ratio of $(V_M + V_B)/V_M$ is 2.8 at $t = 15$ hr in this case, and in Maggi (2009)'s model, this ratio is approximately 1.5–3.0 for biomineral flocs at the Zeebrugge site. Additionally, this study shows that the moment m_0 (which represents total particle number in suspension) rapidly drops off to 0.1% of the initial m_0 under $G = 32$ s^{-1} because of flocculation and then increases every 3 hr since the increments of shear rate from 32 to 90 s^{-1} gradually break up large flocs and release more small particles in the water column, with the floc number m_0 finally raises to 1 % of the initial value under $G = 90$ s^{-1}. In addition, the moments m_1 and m_2 follow, while the moment m_4 (which is proportional to the total surface area of particles falling per unit time; see Mehta, 2013) is opposite to, the tendency of m_0 curve, with an apparent jump at $t = 6$ hr when shear rate changes from 48 to 64 s^{-1}. After increasing to quasi-equilibrium state in the first 1 hr, the mean ($d_{1,0}$) and median (D_{50}) sizes of FSD are descending as shear rate increases (solid lines in Figure 8b). The predicted and experimental $d_{1,0}$ and D_{50} agree well under shear rate $G = \{32, 48, 64, 80\}$ s^{-1} with a maximum error of 12% for $d_{1,0}$ and 9% for D_{50}, although it shows a higher prediction under $G = 96$ s^{-1}. In Shen and Maa (2015)'s simulations, the $d_{1,0}$ and D_{50} reach equilibrium states at $t = \{3, 6, 9, 12, 15\}$ hr before the shear rates change (dashed lines in Figure 8b). Notably at $t = 9$ hr, their model shows a better prediction of $d_{1,0}$ than D_{50}, while this study represents a better match of D_{50} than $d_{1,0}$. The deviations of $d_{1,0}$ and D_{50} indicate that the distribution is skewed and not normal. Note that since Shen and Maa (2015)'s model cannot address the biological part of the biomineral flocs, our modeling approach contributed to a simple description of the biofilms growing on the surfaces of suspended particles in natural environments. Further improvements may be investigated by including intermolecular forces (e.g., van der Waals force and electrostatic repulsive attractive force represented by classical or extended DLVO theory; see Derjaguin & Landau, 1941; Van Van Oss, 2008; Verway & Overbeek, 1948) between mineral particles and biofilms in the correction factor α or the floc strength F_y (Tang et al., 2001; Zhang et al., 2016). By then, our model has the potential to better describe the process and better capture the data.

5.2. Floc Size Interpretation: Multiple Classes and Multiple Peaks?

Knowing how many size classes are preferable to interpret a FSD is still an open question. Since our long-term target is to implement the flocculation model in large-scale estuary and ocean models to improve the predictions of sediment dynamics, using hundreds or thousands of size classes to display a FSD (e.g., Vanni, 2000) is not practical. For example, Sherwood et al. (2018) implemented Verney et al. (2011)'s flocculation model in the Regional Ocean Modeling System (ROMS). Even with size classes less than 20, their application was limited to a one-dimensional vertical case. Only with reduced size classes (e.g., Lee et al., 2011; Shen, Lee, et al., 2018; Shen, Toorman, et al., 2018) has it possibly applied for relatively large domains such as in the Oslo Fjord using the TELEMAC system (http://www.opentelemac.org/).

With a small number of moments, it may be not sufficient to accurately reconstruct the FSDs. For example, Prat and Ducoste (2006) and Marchisio, Vigil, et al., (2003) tracked particle aggregation and breakage with three classes. They did not recover the size distributions from the moments, because three classes are not sufficient to show a meaningful FSD. Instead, Shen and Maa (2015, 2016a) indicated that it is reasonable to use eight classes to recover the FSDs by comparing with both analytical results and kaolinite laboratory experiments. Consequently, although better FSD predictions may be achieved by tracking more moments, only eight classes are selected in this study considering both accuracy and efficiency.

It is striking that the observed FSDs in Tang (2017)'s experiments, even for NABA conditions, only have one major peak. This is in contrast with some measured FSDs in biofilm involved experiments that clearly show multimodal features. For example, Shen and Maa (2016b) have produced bimodal FSDs of kaolinite suspensions with different dosages of guar gum in one of their mixing chamber tests. Multipeak FSDs are also reported in other studies focusing on the effects of organic substances on montmorillonite flocculation with cationic (such as chitosan), neutral (such as guar gum), or anionic (such as xanthan) EPS (Furukawa & Watkins, 2012; Zhang et al., 2013; Tan et al., 2012, 2014; Furukawa et al., 2014). The occurrence of multimodality may be because of heterogeneous particle composition, irregular shaped flocs, limitation of floc size measuring technologies (that refer to spherical particles), and so on. The approaches to better observe and simulate a multipeak FSD are still underway.

5.3. Limitations and Future Directions

It is critical to note that the logistic model (equation (2)) should be used with care for a wider application in the field. Biofilms are comprised mainly of bacteria. Some of the bacteria are heterotrophic organisms, for which the regulating nutrient is dissolved organic carbon instead of DIN. Even for photosynthetic bacteria, the relative growth rate η depends on not only nutrient concentrations but also photosynthesis. Thus, a light intensity term should usually be included, except for short-term laboratory experiments under room light condition such as used in this study. The change of floc size due to biofilm creation in natural waters may also relate to temperature and flow disturbance (Concas et al., 2016; Wang et al., 2016). Incorporating all these impacts into numerical models will significantly increase the model complexity and will make the model forecast also strongly depending on the predictions of water quality parameters. The use of a simple biological model as shown in this study may be a good alternative, as it is efficient in solving the biomediated FSDs. Nevertheless, a comprehensive hydrodynamic-sediment-ecological modeling system to enhance the FSD predictions is still the final target.

Some other studies have focused on the biofilms covering the sediment bed surface (e.g., Droppo, 2009; Fang et al., 2017; Gerbersdorf et al., 2008; Malarkey et al., 2015), and these biofilms could lead to a situation that does not increase suspended flocculation. Contrarily, they could decrease floc size and floc formation by impeding the aggregates and other material being entrained into suspension. Actually, biofilms on and within both bed and suspended sediments influence nearly all sediment processes notably the settling, erosion, and resuspension. With appropriate consideration of other forcings (tide, wave, wind, and surge; e.g., see Brown et al., 2013; Franz et al., 2017; Li et al., 2019; Santoro et al., 2017; Zhang et al., 2017; Zhang et al., 2018) in estuarine and coastal waters, numerical models considering biofilm effects on aggregates could better predict both short-term sediment dynamics and long-term morphological evolutions. This study, nevertheless, only focuses on biofilms around suspended sediment particles.

This model may also have the potential to investigate the dynamics of particles introduced by human activities into the aquatic environment such as microplastics. The transport and fate of microplastics in coastal waters have received increased attention over the last few years (Rummel et al., 2017). The fact that some microplastic particles with densities close to water, not only float on the water surface but are also detected in bottom sediment samples (e.g., Claessens et al., 2011; Coppock et al., 2017; Imhof et al., 2012; Peng et al., 2017), implies that microplastics are deeply involved in the flocculation processes of fine-grained sediments, which are in turn widely hypothesized to be one of the major sinks of the microplastics. It is important to take into consideration the flocculated minerals and the absorbed microplastics and organic particles that interact with each other to predict the FSDs (Ogonowski et al., 2018). The particle dynamics associated with microplastics and natural cohesive sediments are more or less similar, except that fragmentation due to weathering and waves is an additional mechanism to be considered for microplastics. As a consequence, further studies are required to understand the multicomposition aggregates (e.g., plastic-absorbed

sediment flocs) controlled by various physical transport processes (e.g., advection, diffusion, and wind) and biochemical reactions (e.g., flocculation, digestion, and weathering; Zhang, 2017).

6. Conclusions

In this study, the PBE is used to model the FSDs of cohesive sediments in aquatic environments, including the processes of aggregation, breakage, and biofilm growth. The following conclusions are drawn:

1. Besides the aggregation and breakage terms, the effects of biofilm growth are described in the growth term of PBE. The quadrature method of moments is used to solve the PBE. With the adjustable factor selected as $p = 3$, the model is able to represent the observed unimodal FSDs with eight size groups ($N_d = 8$).

2. In the growth term, the biofilm growth rate η is assumed nutrient dependent and following the logistic growth. The maximum specific growth rate $\eta_{\max}$, determined by the comparisons of predicted and measured $D_{50} \sim t$ curve under NABA and NABF conditions, is in the order of $10^{-5}\,\mathrm{s}^{-1}$ in this study. Moreover, the carrying capacity of floc size is assumed to be proportional to the Kolmogorov microscale and thus changes with shear rate.

3. In the flocculation model, different fragmentation distribution functions may be selected to fit the observed FSDs, since the FSDs under low and high shear rates may exhibit different FSD spread. In addition, the collision correction factor may be larger than one for a rapid flocculation, notably when biofilm activities are abundant.

4. This simplified bioflocculation model highlights the increment of representative sizes of FSDs due to biofilm coating. Although complex chemical and biological model may be preferable after a clear understanding of the processes and a robust coding of the wave, sediment, and water qualities, this model, especially at the current stage, has the advantage to rapidly and efficiently apply in estuarine-scale areas in the near future.

References

Barton, A. F., Wallis, M. R., Sargison, J. E., Buia, A., & Walker, G. J. (2008). Hydraulic roughness of biofouled pipes, biofilm character, and measured improvements from cleaning. *Journal of Hydraulic Engineering*, *134*(6), 852–857. https://doi.org/10.1061/(ASCE)0733-9429(2008)134:6(852)

Branda, S. S., Vik, A., Friedman, L., & Kolter, R. (2005). Biofilms: The matrix revisited. *Trends in Microbiology*, *13*(1), 20–26. https://doi.org/10.1016/j.tim.2004.11.006

Brown, J. M., Bolanos, R., & Wolf, J. (2013). The depth-varying response of coastal circulation and water levels to 2D radiation stress when applied in a coupled wave-tide-surge modelling system during an extreme storm. *Coastal Engineering*, *82*, 102–113. https://doi.org/10.1016/j.coastaleng.2013.08.009

Camp, T. R., & Stein, P. C. (1943). Velocity gradients and internal work in fluid motion. *Journal of the Boston Society of Civil Engineers*, *30*, 219–237.

Chen, X. D., Zhang, C. K., Zhou, Z., Gong, Z., Zhou, J. J., Tao, J. F., et al. (2017). Stabilizing effects of bacterial biofilms: EPS penetration and redistribution of bed stability down the sediment profile. *Journal of Geophysical Research: Biogeosciences*, *122*, 3113–3125. https://doi.org/10.1002/2017JG004050

Cheng, P. D., Zhu, H. W., Zhong, B. C., & Wang, D. Z. (2015). Transport mechanisms of contaminants released from fine sediment in rivers. *Acta Mechanica Sinica*, *31*(6), 791–798. https://doi.org/10.1007/s10409-015-0520-8

Claessens, M., De Meester, S., Van Landuyt, L., De Clerck, K., & Janssen, C. R. (2011). Occurrence and distribution of microplastics in marine sediments along the Belgian coast. *Marine Pollution Bulletin*, *62*(10), 2199–2204. https://doi.org/10.1016/j.marpolbul.2011.06.030

Concas, A., Pisu, M., & Cao, G. (2016). A novel mathematical model to simulate the size-structured growth of microalgae strains dividing by multiple fission. *Chemical Engineering Journal*, *287*, 252–268. https://doi.org/10.1016/j.cej.2015.11.021

Coppock, R. L., Cole, M., Lindeque, P. K., Queiros, A. M., & Galloway, T. S. (2017). A small-scale, portable method for extracting microplastics from marine sediments. *Environmental Pollution*, *230*, 829–837. https://doi.org/10.1016/j.envpol.2017.07.017

Decho, A. W., & Gutierrez, T. (2017). Microbial extracellular polymeric substances (EPSs) in ocean systems. *Frontiers in Microbiology*, *8*(922). https://doi.org/10.3389/fmicb.2017.00922

Decho, A. W., Kawaguchi, T., Allison, M. A., Louchard, E. M., Reid, R. P., Stephens, F. C., et al. (2003). Sediment properties influencing upwelling spectral reflectance signatures: The "biofilm gel effect". *Limnology and Oceanography*, *48*(1part2), 431–443. https://doi.org/10.4319/lo.2003.48.1_part_2.0431

Delauney, L., Compère, C., & Lehaitre, M. (2010). Biofouling protection for marine environmental sensors. *Ocean Science*, *6*(2), 503–511. https://doi.org/10.5194/os-6-503-2010

Derjaguin, B., & Landau, L. (1941). Theory of the stability of strongly charged lyophobic sols and of the adhesion of strongly charged particles in solutions of electrolytes. *Acta Physicochim. USSR*, *14*, 633–662.

Downing, J. (2006). Twenty-five years with OBS sensors: The good, the bad, and the ugly. *Continental Shelf Research*, *26*(17-18), 2299–2318. https://doi.org/10.1016/j.csr.2006.07.018

Droppo, I. G. (2009). Biofilm structure and bed stability of five contrasting freshwater sediments. *Marine and Freshwater Research*, *60*(7), 690–699. https://doi.org/10.1071/MF08019

Droppo, I. G., Krishnappan, B. G., & Lawrence, J. R. (2016). Microbial interactions with naturally occurring hydrophobic sediments: Influence on sediment and associated contaminant mobility. *Water Research*, *92*, 121–130. https://doi.org/10.1016/j.watres.2016.01.034

Dyer, K. R. (1989). Sediment processes in estuaries: Future research requirements. *Journal of Geophysical Research*, *94*(C10), 14,327–14,339. https://doi.org/10.1029/JC094iC10p14327

Fang, H. W., Lai, H. J., Cheng, W., Huang, L., & He, G. J. (2017). Modeling sediment transport with an integrated view of the biofilm effects. *Water Resources Research*, *53*, 7536–7557. https://doi.org/10.1002/2017WR020628

Fettweis, M., & Baeye, M. (2015). Seasonal variation in concentration, size and settling velocity of muddy marine flocs in the benthic boundary layer. *Journal of Geophysical Research: Oceans*, *120*, 5648–5667. https://doi.org/10.1002/2014JC010644

Fettweis, M., Baeye, M., Cardoso, C., Dujardin, A., Lauwaert, B., Van den Eynde, D., et al. (2016). The impact of disposal of fine-grained sediments from maintenance dredging works on SPM concentration and fluid mud in and outside the harbor of Zeebrugge. *Ocean Dynamics*, *66*(11), 1497–1516. https://doi.org/10.1007/s10236-016-0996-1

Flemming, H. C. (1998). Relevance of biofilms for the biodeterioration of surfaces of polymeric materials. *Polymer Degradation and Stability*, *59*(1-3), 309–315. https://doi.org/10.1016/S0141-3910(97)00189-4

Flemming, H. C., Neu, T. R., & Wozniak, D. J. (2007). The EPS matrix: The "house of biofilm cells". *Journal of Bacteriology*, *189*(22), 7945–7947. https://doi.org/10.1128/JB.00858-07

Franz, G., Delpey, M. T., Brito, D., Pinto, L., Leitao, P., & Neves, R. (2017). Modelling of sediment transport and morphological evolution under the combined action of waves and currents. *Ocean Science*, *13*(5), 673–690. https://doi.org/10.5194/os-13-673-2017

Furukawa, Y., Reed, A. H., & Zhang, G. (2014). Effect of organic matter on estuarine flocculation: a laboratory study using montmorillonite, humic acid, xanthan gum, guar gum and natural estuarine flocs. *Geochemical Transactions*, *15*(1), 1. https://doi.org/10.1186/1467-4866-15-1

Furukawa, Y., & Watkins, J. L. (2012). Effect of organic matter on the flocculation of colloidal montmorillonite: A modeling approach. *Journal of Coastal Research*, *28*(3), 726–737. https://doi.org/10.2112/JCOASTRES-D-11-00128.1

Gerbersdorf, S. U., Jancke, T., Westrich, B., & Paterson, D. M. (2008). Microbial stabilization of riverine sediments by extracellular polymeric substances. *Geobiology*, *6*, 57–69. https://doi.org/10.1111/j.1472-4669.2007.00120.x

Gibbs, R. J., & Wolanski, E. (1992). The effect of flocs on optical backscattering measurements of suspended material concentration. *Marine Geology*, *107*(4), 289–291. https://doi.org/10.1016/0025-3227(92)90078-V

Guo, C., He, Q., Guo, L., & Winterwerp, J. C. (2017). A study of in-situ sediment flocculation in the turbidity maxima of the Yangtze Estuary. *Estuarine Coastal and Shelf Science*, *191*, 1–9. https://doi.org/10.1016/j.ecss.2017.04.001

Hoiby, N. (2017). A short history of microbial biofilms and biofilm infections. *APMIS*, *125*(4), 272–275. https://doi.org/10.1111/apm.12686

Huang, Z., McLamore, E. S., Chuang, H. S., Zhang, W., Wereley, S., Leon, J. L. C., & Banks, M. K. (2013). Shear-induced detachment of biofilms from hollow fiber silicone membranes. *Biotechnology and Bioengineering*, *110*(2), 525–534. https://doi.org/10.1002/bit.24631

Imhof, H. K., Schmid, J., Niessner, R., Ivleva, N. P., & Laforsch, C. (2012). A novel, highly efficient method for the separation and quantification of plastic particles in sediments of aquatic environments. *Limnology and Oceanography: Methods*, *10*(7), 524–537. https://doi.org/10.4319/lom.2012.10.524

Jachlewski, S., Jachlewski, W. D., Linne, U., Brasen, C., Wingender, J., & Siebers, B. (2015). Isolation of extracellular polymeric substances from biofilms of the thermoacidophilic archaeon *Sulfolobus acidocaldarius*. *Frontiers in Bioengineering and Biotechnology*, *3*, 123. https://doi.org/10.3389/fbioe.2015.00123

Jiang, Q., & Logan, B. E. (1991). Fractal dimensions of aggregates determined from steady-state size distributions. *Environmental Science & Technology*, *25*(12), 2031–2038. https://doi.org/10.1021/es00024a007

Kerr, A., Cowling, M. J., Beveridge, C. M., Smith, M. J., Parr, A. C. S., Head, R. M., et al. (1998). The early stages of marine biofouling and its effects on two types of optical sensors. *Environment International*, *24*(3), 331–343. https://doi.org/10.1016/S0160-4120(98)00011-7

Keyvani, A., & Strom, K. (2014). Influence of cycles of high and low turbulent shear on the growth rate and equilibrium size of mud flocs. *Marine Geology*, *354*, 1–14. https://doi.org/10.1016/j.margeo.2014.04.010

Kucharavy, D., & De Guio, R. (2015). Application of logistic growth curve. *Procedia Engineering*, *131*, 280–290. https://doi.org/10.1016/j.proeng.2015.12.390

Kuprenas, R., Tran, D., & Strom, K. (2018). A shear-limited flocculation model for dynamically predicting average floc size. *Journal of Geophysical Research: Oceans*, *123*(9), 6736–6752. https://doi.org/10.1029/2018JC014154

Lai, H., Fang, H., Huang, L., He, G., & Reible, D. (2018). A review on sediment bioflocculation: Dynamics, influencing factors and modeling. *Science of The Total Environment*, *642*, 1184–1200. https://doi.org/10.1016/j.scitotenv.2018.06.101

Lee, B. J., Toorman, E., Molz, F. J., & Wang, J. (2011). A two-class population balance equation yielding bimodal flocculation of marine or estuarine sediments. *Water Research*, *45*(5), 2131–2145. https://doi.org/10.1016/j.watres.2010.12.028

Lee, D. G., Bonner, J. S., Garton, L. S., Ernest, A. N. S., & Autenrieth, B. L. (2000). Modeling coagulation kinetics incorporating fractal theories: a fractal rectilinear approach. *Water Research*, *34*(7), 1987–2000. https://doi.org/10.1016/S0043-1354(99)00354-1

Lefebvre, S., Mouget, J. C., & Lavaud, J. (2011). Duration of rapid light curves for determining the photosynthetic activity of microphytobenthos biofilm *in situ*. *Aquatic Botany*, *95*(1), 1–8. https://doi.org/10.1016/j.aquabot.2011.02.010

Li, X., Dai, L. G., Zhang, C., Zeng, G. M., Liu, Y. G., Zhou, C., et al. (2017). Enhanced biological stabilization of heavy metals in sediment using immobilized sulfate reducing bacteria beads with inner cohesive nutrient. *Journal of Hazardous Materials*, *324*(Pt B), 340–347. https://doi.org/10.1016/j.jhazmat.2016.10.067

Li, X., Leonardi, N., & Plater, A. J. (2019). Wave-driven sediment resuspension and salt marsh frontal erosion alterthe export of sediments from macro-tidal estuaries. *Geomorphology*, *325*, 17–28. https://doi.org/10.1016/j.geomorph.2018.10.004

Lintern, D.G. (2003). Influences of flocculation on bed properties for fine-grained cohesive sediment (Doctoral dissertation). United Kingdom: Oxford University.

Maggi, F. (2009). Biological flocculation of suspended particles in nutrient-rich aqueous ecosystems. *Journal of Hydrology*, *376*(1-2), 116–125. https://doi.org/10.1016/j.jhydrol.2009.07.040

Maggi, F., Mietta, F., & Winterwerp, J. C. (2007). Effect of variable fractal dimension on the floc size distribution of suspended cohesive sediment. *Journal of Hydrology*, *343*(1-2), 43–55. https://doi.org/10.1016/j.jhydrol.2007.05.035

Malarkey, J., Bass, J. H., Hope, J. A., Aspden, R. J., Parsons, D. R., Peakall, J., et al. (2015). The pervasive role of biological cohesion in bedform development. *Nature Communications*, *6*(1), 6257. https://doi.org/10.1038/ncomms7257

Marchisio, D. L., Pikturna, J. T., Fox, R. O., Vigil, R. D., & Barresi, A. A. (2003). Quadrature method of moments for population-balance equations. *AIChE Journal*, *49*(5), 1266–1276. https://doi.org/10.1002/aic.690490517

Marchisio, D. L., Vigil, R. D., & Fox, R. O. (2003). Quadrature method of moments for aggregation-breakage processes. *Journal of Colloid and Interface Science*, *258*(2), 322–334. https://doi.org/10.1016/S0021-9797(02)00054-1

McGraw, R. (1997). Description of aerosol dynamics by the quadrature method of moments. *Aerosol Science and Technology*, *27*(2), 255–265 . https://doi.org/10.1080/02786829708965471

Mehta, A. J. (2013). *An introduction to hydraulics of fine sediment transport*. New Jersey: World Scientific Publishing Company. https://doi. org/10.1142/8708

Metosh-Dickey, C. A., Portier, R. J., & Xie, X. G. (2004). A novel surface coating incorporating copper metal flakes for reducing biofilm attachment. *Materials Performance*, *43*, 30–34.

Mietta, F., Maggi, F., & Winterwerp, J. C. (2008). Chapter 19 Sensitivity to breakup functions of a population balance equation for cohesive sediments. In *Proceedings in Marine Science*, (Vol. 9, pp. 275–286). Amsterdam: Elsevier. https://doi.org/10.1016/S1568-2692(08)80021-6

Monod, J. (1949). The growth of bacterial cultures. *Annual Reviews in Microbiology*, *3*(1), 371–394. https://doi.org/10.1146/annurev. mi.03.100149.002103

Ogonowski, M., Gerdes, Z., & Gorokhova, E. (2018). What we know and what we think we know about microplastic effects—A critical perspective. *Current Opinion in Environmental Science & Health*, *1*, 41–46. https://doi.org/10.1016/j.coesh.2017.09.001

Peng, G., Zhu, B., Yang, D., Su, L., Shi, H., & Li, D. (2017). Microplastics in sediments of the Changjiang Estuary, China. *Environmental Pollution*, *225*, 283–290. https://doi.org/10.1016/j.envpol.2016.12.064

Prakash, B., Veeregowda, B. M., & Krishnappa, G. (2003). Biofilms: A survival strategy of bacteria. *Current Science*, *85*, 1299–1307.

Prat, O. P., & Ducoste, J. J. (2006). Modeling spatial distribution of floc size in turbulent processes using the quadrature method of moment and computational fluid dynamics. *Chemical Engineering Science*, *61*(1), 75–86. https://doi.org/10.1016/j.ces.2004.11.070

Quigg, A., Passow, U., Chin, W. C., Xu, C., Doyle, S., Bretherton, L., et al. (2016). The role of microbial exopolymers in determining the fate of oil and chemical dispersants in the ocean. *Limnology and Oceanography Letters*, *1*(1), 3–26. https://doi.org/10.1002/ lol2.10030

Riebesell, U. (1991). Particle aggregation during a diatom bloom. 2. Biological aspects. *Marine Ecology Progress Series*, *69*, 281–291. https:// www.jstor.org/stable/24816840, https://doi.org/10.3354/meps069281

Rummel, C. D., Jahnke, A., Gorokhova, E., Kühnel, D., & Schmitt-Jansen, M. (2017). Impacts of biofilm formation on the fate and potential effects of microplastic in the aquatic environment. *Environmental Science & Technology Letters*, *4*(7), 258–267. https://doi.org/10.1021/ acs.estlett.7b00164

Saint-Béat, B., Dupuy, C., Agogué, H., Carpentier, A., Chalumeau, J., Como, S., et al. (2014). How does the resuspension of the biofilm alter the functioning of the benthos-pelagos coupled food web of a bare mudflat in Marennes-Oléron Bay (NE Atlantic)? *Journal of Sea Research*, *92*, 144–157. https://doi.org/10.1016/j.seares.2014.02.003

Santoro, P., Fossati, M., Tassi, P., Huybrechts, N., Bang, D. P. V., & Piedra-Cueva, J. C. I. (2017). A coupled wave-current-sediment transport model for an estuarine system: Application to the Rio de la Plata and Montevideo Bay. *Applied Mathematical Modelling*, *52*, 107–130. https://doi.org/10.1016/j.apm.2017.07.004

Shaw, D. J. (1992). *Introduction to colloid and surface chemistry*. London: Butterworth-Heinemann.

Shen, X. (2016). Modeling flocculation and deflocculation processes of cohesive sediments (Doctoral dissertation). Gloucester Point, VA: Virginia Institute of Marine Science, School of Marine Science, College of William & Mary.

Shen, X., Lee, B. J., Fettweis, M., & Toorman, E. A. (2018). A tri-modal flocculation model coupled with TELEMAC for estuarine muds both in the laboratory and in the field. *Water Research*, *145*, 473–486. https://doi.org/10.1016/j.watres.2018.08.062

Shen, X., & Maa, J. P. Y. (2015). Modeling floc size distribution of suspended cohesive sediments using quadrature method of moments. *Marine Geology*, *359*, 106–119. https://doi.org/10.1016/j.margeo.2014.11.014

Shen, X., & Maa, J. P. Y. (2016a). Numerical simulations of particle size distributions: Comparison with analytical solutions and kaolinite flocculation experiments. *Marine Geology*, *379*, 84–99. https://doi.org/10.1016/j.margeo.2016.05.014

Shen, X., & Maa, J. P. Y. (2016b). A camera and image processing system for floc size distributions of suspended particles. *Marine Geology*, *376*, 132–146. https://doi.org/10.1016/j.margeo.2016.03.009

Shen, X., & Maa, J. P. Y. (2017). Floc size distributions of suspended kaolinite in an advection transport dominated tank: Measurements and modeling. *Ocean Dynamics*, *67*(11), 1495–1510. https://doi.org/10.1007/s10236-017-1097-5

Shen, X., Toorman, E. A., Lee, B. J., & Fettweis, M. (2018). Biophysical flocculation of suspended particulate matters in Belgian coastal zones. *Journal of Hydrology*, *567*, 238–252. https://doi.org/10.1016/j.jhydrol.2018.10.028

Sherwood, C. R., Aretxabaleta, A. L., Harris, C. K., Rinehimer, J. P., Verney, R., & Ferré, B. (2018). Cohesive and mixed sediment in the Regional Ocean Modeling System (ROMS v3.6) implemented in the Coupled Ocean-Atmosphere-Wave-Sediment Transport Modeling System (COAWST r1234). *Geoscientific Model Development*, *11*(5), 1849–1871. https://doi.org/10.5194/gmd-11-1849-2018

Sobeck, D. C., & Higgins, M. J. (2002). Examination of three theories for mechanisms of cation-induced bioflocculation. *Water Research*, *36*(3), 527–538. https://doi.org/10.1016/S0043-1354(01)00254-8

Song, D. H., & Wang, X. H. (2013). Suspended sediment transport in the Deepwater Navigation Channel, Yangtze River Estuary, China, in the dry season 2009: 2. *Numerical simulations. Journal of Geophysical Research: Oceans*, *118*(10), 5555–5567. https://doi.org/10.1002/ jgrc.20410

Su, J. W., Gu, Z. L., Li, Y., Feng, S. Y., & Xu, X. Y. (2007). Solution of population balance equation using quadrature method of moments with an adjustable factor. *Chemical Engineering Science*, *62*(21), 5897–5911. https://doi.org/10.1016/j.ces.2007.06.016

Tan, X., Hu, L., Reed, A. H., Furukawa, Y., & Zhang, G. (2014). Flocculation and particle size analysis of expansive clay sediments affected by biological, chemical, and hydrodynamic factors. *Ocean Dynamics*, *64*(1), 143–157. https://doi.org/10.1007/s10236-013-0664-7

Tan, X., Zhang, G., Yin, H., Reed, A. H., & Furukawa, Y. (2012). Characterization of particle size and settling velocity of cohesive sediments affected by a neutral exopolymer. *International Journal of Sediment Research*, *27*(4), 473–485. https://doi.org/10.1016/S1001-6279(13)60006-2

Tang, F.H.M. (2017). Microbiological modulation of suspended particulate matter dynamics (Doctoral dissertation). Australia: University of Sydney.

Tang, F.H.M., & Maggi, F. (2015). A laboratory facility for flocculation-related experiments. The University of Sydney. Report No. R952.

Tang, F. H. M., & Maggi, F. (2016). A mesocosm experiment of suspended particulate matter dynamics in nutrient- and biomass-affected waters. *Water Research*, *89*, 76–86. https://doi.org/10.1016/j.watres.2015.11.033

Tang, F. H. M., & Maggi, F. (2018). Biomodulation of nitrogen cycle in suspended sediment. *Journal of Geophysical Research: Biogeosciences*, *123*(4), 1230–1246. https://doi.org/10.1002/2017JG004165

Tang, S., Ma, Y., & Shiu, C. (2001). Modelling the mechanical strength of fractal aggregates. *Colloids and Surfaces A: Physicochemical and Engineering Aspects*, *180*(1-2), 7–16. https://doi.org/10.1016/S0927-7757(00)00743-3

Tran, D., & Strom, K. (2017). Suspended clays and silts: Are they independent or dependent fractions when it comes to settling in a turbulent suspension? *Continental Shelf Research*, *138*, 81–94. https://doi.org/10.1016/j.csr.2017.02.011

Tsoularis, A., & Wallace, J. (2002). Analysis of logistic growth models. *Mathematical Biosciences*, *179*(1), 21–55. https://doi.org/10.1016/S0025-5564(02)00096-2

Van Leussen, W. (1988). Aggregation of particles, settling velocity of mudflocs: a review. In J. Dronkers, & W. Van Leussen (Eds.), *Physical Processes in Estuaries. SpringerVerlag*, (pp. 347–403). Berlin. https://doi.org/10.1007/978-3-642-73691-9_19

Van Leussen, W. (1994). Estuarine macroflocs and their role in fine-grained sediment transport (Doctoral dissertation). Netherlands: University of Utrecht.

Van Oss, C. J. (2008). Chapter three—The extended DLVO theory. *Interface Science and Technology*, *16*, 31–48. https://doi.org/10.1016/S1573-4285(08)00203-2

Vanni, M. (2000). Approximate population balance equations for aggregation-breakage processes. *Journal of Colloid and Interface Science*, *221*(2), 143–160. https://doi.org/10.1006/jcis.1999.6571

Verney, R., Lafite, R., Brun-Cottan, J. C., & Le Hir, P. (2011). Behaviour of a floc population during a tidal cycle: Laboratory experiments and numerical modelling. *Continental Shelf Research*, *31*(10), S64–S83. https://doi.org/10.1016/j.csr.2010.02.005

Verway, E. J., & Overbeek, J. T. G. (1948). *Theory of the stability of lyophobic colloids*. New York: Elsevier Publishing Company, Inc.

Wang, H., Zhou, Y., Xia, K., Yang, R., & Liu, X. (2016). Flow-disturbance considered simulation for algae growth in a river-lake system. *Ecohydrology*, *9*(4), 601–609. https://doi.org/10.1002/eco.1659

Watnick, P., & Kolter, R. (2000). Biofilm, city of microbes. *Journal of Bacteriology*, *182*(10), 2675–2679. https://doi.org/10.1128/JB.182.10.2675-2679.2000

Wheeler, J. C. (1974). Modified moments and Gaussian quadratures. *Journal of Mathematics*, *4*, 287–296. https://www.jstor.org/stable/44237566

Winterwerp, J. C. (1998). A simple model for turbulence induced flocculation of cohesive sediment. *Journal of Hydraulic Research*, *36*(3), 309–326. https://doi.org/10.1080/00221689809498621

Yuan, C., & Fox, R. O. (2011). Conditional quadrature method of moments for kinetic equations. *Journal of Computational Physics*, *230*(22), 8216–8246. https://doi.org/10.1016/j.jcp.2011.07.020

Zhang, C., Zhang, Q., Zheng, J., & Demirbilek, Z. (2017). Parameterization of nearshore wave front slope. *Coastal Engineering*, *127*, 80–87. https://doi.org/10.1016/j.coastaleng.2017.06.008

Zhang, G., Yin, H., Lei, Z., Reed, A. H., & Furukawa, Y. (2013). Effects of exopolymers on particle size distributions of suspended cohesive sediments. *Journal of Geophysical Research: Oceans*, *118*, 3473–3489. https://doi.org/10.1002/jgrc.20263

Zhang, H. (2017). Transport of microplastics in coastal seas. *Estuarine Coastal and Shelf Science*, *199*, 74–86. https://doi.org/10.1016/j.ecss.2017.09.032

Zhang, J., Maa, J. P. Y., Zhang, Q., & Shen, X. (2016). Direct numerical simulations of collision efficiency of cohesive sediments. *Estuarine Coastal and Shelf Science*, *178*, 92–100. https://doi.org/10.1016/j.ecss.2016.06.003

Zhang, J., Shen, X., Zhang, Q., Maa, J. P.-Y., & Qiao, G. (2019). Bimodal particle size distributions of fine-grained cohesive sediments in a settling column with oscillating grids. *Continental Shelf Research*, *174*, 85–94. https://doi.org/10.1016/j.csr.2019.01.005

Zhang, W., Cao, Y., Zhu, Y., Zheng, J., Ji, X., Xu, Y., et al. (2018). Unravelling the causes of tidal asymmetry in deltas. *Journal of Hydrology*, *564*, 588–604. https://doi.org/10.1016/j.jhydrol.2018.07.023

Zhao, H., Fang, H., Nakagawa, H., & Zhang, H. (2012). An overview of microbial interactions with sediment dynamics. Japan-China Symposium on Advances in Water and Sediment Research, Kyoto, Japan, July 30–August 1.

Ziegler, S., & Lyon, D. R. (2010). Factors regulating epilithic biofilm carbon cycling and release with nutrient enrichment in headwater streams. *Hydrobiologia*, *657*(1), 71–88. https://doi.org/10.1007/s10750-010-0296-6

Zobell, C. E., & Allen, E. C. (1935). The significance of marine bacteria in the fouling of submerged surfaces. *Journal of Bacteriology*, *29*(3), 239–251.